

Supporting Information †

Oxygen incorporated WS₂ Nanoclusters with Superior Electrocatalytic Properties for Hydrogen Evolution Reaction

*Prasad V. Sarma,¹ Chandra Sekhar Tiwary,² Sruthi Radhakrishnan,² Pulickel M. Ajayan² and
Manikoth M. Shaijumon^{1,*}*

¹ School of Physics, Indian Institute of Science Education and Research Thiruvananthapuram,
Maruthamala PO, Thiruvananthapuram, Kerala, 695551, India

² Department of Materials Science and NanoEngineering, Rice University, 6100 Main St,
Houston, TX 77005, United States.
E-mail: shaiju@iisertvm.ac.in

Contents

1. Experimental section details
2. Fig. S1: SEM, XRD, Raman spectra and XPS from WO_{3-x} rods
3. Fig. S2: SEM, XRD and Raman spectra from O-WS₂
4. Fig. S3: EELS elemental mapping images from O-WS₂-1T nanoclusters
5. Fig. S4: AFM height profile images from O-WS₂-1T and O-WS₂-2H nanoclusters
6. Fig. S5: SEM, TEM and HR TEM images of WS₂-BM 1T and 2H nanoclusters
7. Fig. S6: SEM, TEM and HR TEM images of WS₂-P-1T and WS₂-P-2H sheets
8. Fig. S7: Raman spectra collected from WS₂-BM-1T, WS₂-BM-2H, WS₂-P-1T and WS₂-
P-2H samples
9. Fig. S8: XPS spectra from WS₂-BM-1T, WS₂-BM-2H, WS₂-P-1T and WS₂-P-2H
samples
10. Fig. S9: XPS S2p and O1s spectra from O-WS₂-1T and O-WS₂-2H nanoclusters

11. Fig. S10: XPS wide scan from various catalysts
12. Fig. S11: PEIS spectra obtained from catalysts under study
13. Fig. S12: Cyclic voltammogram in 5 mM $K_3[Fe(CN)_6]$ in 0.1M KCl
14. Fig. S13: Cyclic voltammogram in 5 mM $[Ru(NH_3)_6]Cl_3$ in 0.1M KCl
15. Fig. S14: Polarization Plot normalized by ECSA- Randles-Sevcik method
16. Fig. S15: Double layer capacitance calculations through Cyclic voltammetry
17. Fig. S16: Polarization Plot normalized by ECSA-Double layer capacitance method
18. Fig. S17: SEM, TEM images and Raman spectra collected from WO_3 - WS_2 -1T and WO_3 - WS_2 -2H nanoclusters
19. Fig. S18: XPS spectra obtained from WO_3 - WS_2 -1T and WO_3 - WS_2 -2H nanoclusters
20. Fig. S19: Polarization and Tafel plot from WO_3 - WS_2 -1T and WO_3 - WS_2 -2H nanoclusters

1. Experimental Section

1.a Synthesis of WO_{3-x} rods: An aqueous solution containing a mixture of 1.32 g of $(NH_4)_{10}W_{12}O_{41} \cdot 7H_2O$ and 2.10 g of citric acid was heated to 120 °C under constant stirring for 4–5 h until a gel was formed. This formed gel was allowed to stand overnight. 2.45 g of hexadecyl amine dissolved in ethanol was added as an additive to the gel and stirred for 10 h. The resulting mixture was transferred to a 40 ml Teflon autoclave with a stainless steel protective outer body and heated at 200 °C for four days.¹ The product obtained was washed with ethanol, cyclohexane, water and finally with ethanol and dried at room temperature. The synthesized compound is in blue color.

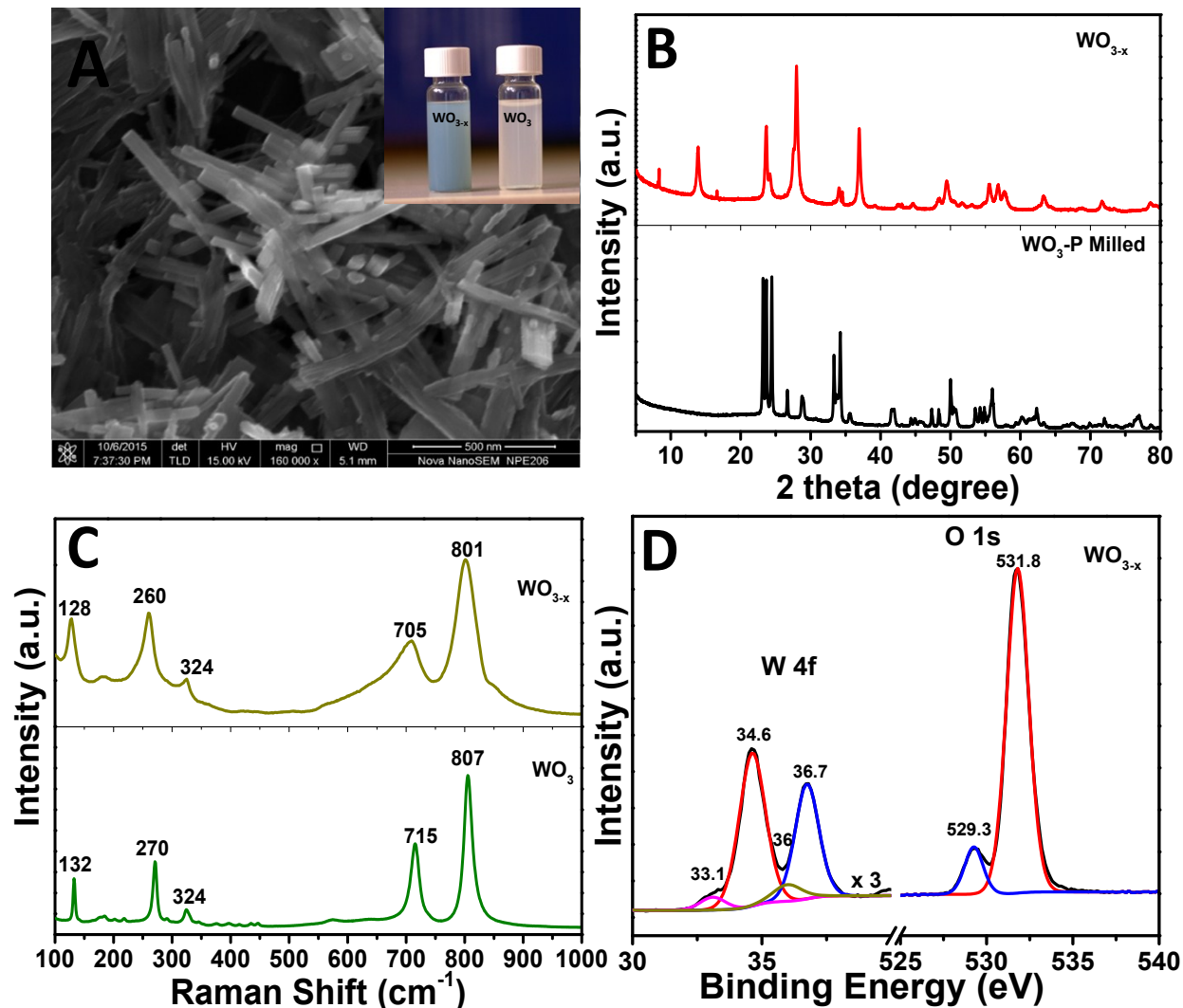


Fig. S1: (A) SEM image of synthesized WO_{3-x} rods. The inset shows a photograph of WO_{3-x} rods and WO_3 bulk powder in ethanol (B) XRD from synthesized WO_{3-x} rods and WO_3 pristine powder (C) Raman spectra collected from WO_{3-x} rod compared with WO_3 -Pristine powder where the peaks of WO_{3-x} rods were down shifted (D) XPS spectra of WO_{3-x} rods.

Raman spectra of WO_{3-x} and WO_3 pristine powder is compared in Figure S1C. Raman spectra of WO_{3-x} rods is shown in Figure S1C where characteristic O-W-O stretching modes of WO_6 octahedral units are found to be red shifted compared to that of WO_3 pristine powder. Further, broadening of Raman peaks are observed, which could be due to the lower oxygen/metal ratio and the variation in stoichiometry.² Since W-O bonds in WO_{3-x} are weaker than the bonds involving W^{6+} ions, their corresponding Raman peaks appear at lower energies.³

XPS spectra of WO_{3-x} compound is shown as Figure S1D. XPS spectra for WO_{3-x} show four different peaks of W 4f at 33.1 eV, 34.6 eV, 36 eV and 36.7 eV, indicative of presence of mixed oxides, of which 34.6 eV and 36.7 eV are predominant. But Stoichiometric Tungsten oxide (WO_3) shows characteristic W $4f_{7/2}$ and $4f_{5/2}$ peaks at 35.5 eV and 37.7 eV respectively.⁴ Thus XPS results confirms that the compound exists in WO_{3-x} ($0 < x < 1$) phase.^{5, 6} Further, O 1S spectra show peaks at 531.8 eV and 529.3 eV, which could be attributed to the presence of oxygen in hydroxyl (OH) group⁷ and that of W^{5+} -O bond in WO_{3-x} , respectively. Due to the change in coordination configuration of Tungsten with Oxygen in partial oxides, W-O peak is observed at lower binding energy compared with stoichiometric WO_3 compound.⁸⁻¹⁰

1.b WO_{3-x} rods to WS_2 (Oxygen incorporated WS_2 flakes): These synthesized WO_{3-x} rods were ground with thiourea and kept inside the tubular furnace and heated to 1000 °C. H_2S gas is allowed to pass through the furnace above 500 °C, and for efficient conversion, temperature dwelled at 1000 °C for 15min. The morphology of WO_{3-x} rods before and after H_2S treatment was shown in Fig. S1A and Fig. S2A respectively. The XRD and Raman of the synthesized material were shown in Fig. S2B & C respectively. XRD matches with WS_2 pristine that illustrates the conversion from WO_{3-x} to WS_2 phase is efficient at higher temperatures, and a low intense (002) peak indicates the smaller particle dimension compared to bulk. The predominant Raman peaks at 347 cm^{-1} and 416 cm^{-1} indicate the characteristic WS_2 in plane E^{1}_{2g} and out of plane A_{1g} vibrations respectively.¹¹

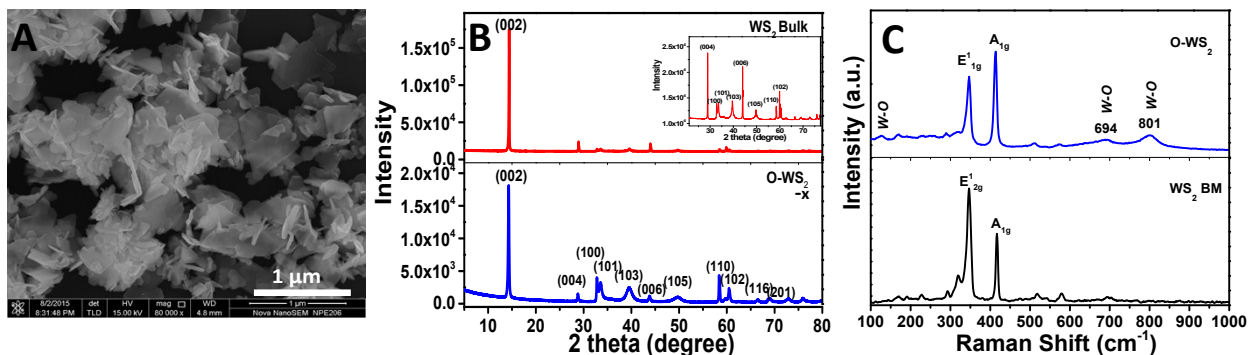


Fig. S2: (A) SEM image of H_2S treated WO_{3-x} rods (O-WS_2) (B) XRD of H_2S treated WO_{3-x} rods compared with bulk WS_2 powder (C) Raman Spectra collected from O-WS_2 and ball milled WS_2 bulk powder. W-O stretching mode vibrations are observed in the O-WS_2 nanostructure.

2. Electrocatalyst preparation

Synthesis of O-WS₂-1T and O-WS₂-2H were mentioned in main text.

Raman spectra of O-WS₂, O-WS₂-1T, and O-WS₂-2H compounds were shown in Fig. 3 where the H₂S treated WO_{3-x} showing high intense W-O vibrations in the high-frequency region. In addition to the characteristic Raman shifts at 347 and 415.6 cm⁻¹, O-WS₂ showing W-O-W Raman vibrations at 690 cm⁻¹ and 801 cm⁻¹ which are slightly shifted compared to those observed for WO_{3-x} nanorods. The Raman peak at 690 cm⁻¹ is reported for h-WO₃, but the conversion from WO_{3-x} to hexagonal-oxide during Sulfidation is not clear. And milled WS₂ flakes show no oxidation even after 6 hrs of high energy ball milling (Fig. 3E).

The spectrum of O-WS₂-2H shows the characteristic 2H-WS₂ peaks corresponding to E_{12g}¹ and A_{1g} at 348 cm⁻¹ and 416 cm⁻¹, respectively. In addition to these characteristic peaks, W-O peaks are also observable at 128 cm⁻¹ and 260 cm⁻¹. And the spectrum of O-WS₂-1T exhibits weak peaks in the lower frequency region, referred as J₁, J₂, J₃ corresponding to the modes that are active only in 1T-WS₂.¹² Here, the peak corresponds to A_{1g} mode seems to be downshifted, and E_{12g}¹ is absent. This behavior is previously reported in the case of MoS₂ monolayer suspension prepared through Lithium intercalation. This absence of peak attributed to the existence of metastable octahedral coordination.¹³

3. WS₂-1T and 2H synthesis

3.a Synthesised from WS₂ Bulk: WS₂ pristine powder ball milled for 6 hours at 600 rpm in Argon atmosphere. Fig. S5A and S5B shows WS₂-Pristine powder before and after milling. Raman spectra of milled WS₂ shows no W-O characteristic peaks given as Fig. 3A. This milled powder chemically exfoliated to obtain 1T NPs (WS₂-BM-1T) using n-butyl lithium and sonicated & refluxed to obtain 2H NPs (WS₂-BM-2H). Fig. S5C and S5D show low and HR-

TEM image of WS₂-BM-1T nanoparticles respectively, and Fig. S5E & S5F shows that of 2H nanoparticles. Raman spectra from 1T and 2H nanoclusters were shown in Fig. S7. XPS from these NPs are shown in Fig. S8, and WS₂-BM-1T Tungsten 4f peaks are downshifted to lower binding energy compared to 2H NPs.

Similarly, WS₂ 1T sheets were prepared from pristine WS₂ powder by chemical exfoliation using n-Butyl lithium and 2H WS₂ sheets were synthesized by sonication method. TEM and SEM images of 1T and 2H sheets were shown in Fig. S6. Raman and XPS spectra from 1T and 2H sheets were shown in Fig. S7 and S8 respectively.

Raman spectra of WS₂-BM-1T & 2H, WS₂-P-1T (1T sheets) WS₂-P-2H (2H sheets) were shown in Fig. S8. Raman spectra of chemically exfoliated nanoclusters and sheets were showing 1T phase (Fig. S 7A and S 7B) while liquid phase exfoliated samples showing characteristic 2H WS₂ peaks. Raman spectra from controllably annealed WS₂-P-1T shows (Fig. S7D) the phase transition from 1T to 2H with an increase in annealing temperature.

3.b Synthesised from WO₃ Bulk: Synthesis of WO₃-WS₂-1T and WO₃-WS₂-2H nanoclusters were given in main text. SEM images of WO₃ before and after ball milling and after H₂S treatment were shown in Fig. S17A, B, and C respectively. Later WO₃-WS₂ is chemically exfoliated to obtain 1T nanoclusters. And liquid phase exfoliated to obtain WO₃-WS₂-2H nanoclusters. Low-resolution TEM images of 1T and 2H nanoclusters were shown in Fig. S17D and S17E respectively. Raman shown in Fig. S17F indicates the absence of oxides in the synthesized compound. Raman signal from WO₃-WS₂-1T indicated the phase transition to 1T polymorph. XPS from 1T and 2H nanoclusters were illustrated in Fig. S18. 2H WS₂ NPs shows W 4f peaks at 33 eV and 35.1 eV, and for 1T WS₂, a negative shift in Tungsten W4f peaks (32.4 eV & 34.45 eV) confirms the metallic phase of WS₂.

HER studies were conducted on $\text{WO}_3\text{-WS}_2\text{-1T}$ and 2H nanoclusters by following similar methods mentioned above. Polarization curve and Tafel plots were shown in Fig. S19. The onset potential of $\text{WS}_2\text{-WO}_3\text{-1T}$ shows an onset potential of 157 mV and a Tafel slope of 76 mV dec^{-1} . Similarly, $\text{WS}_2\text{-WO}_3\text{-2H}$ illustrates 312 mV and 98 mV dec^{-1} onset potential and Tafel slope respectively. The performances of $\text{WO}_3\text{-WS}_2\text{-1T}$ phase is better compared to 2H but these all fall behind $\text{O-WS}_2\text{-T}$ catalysts.

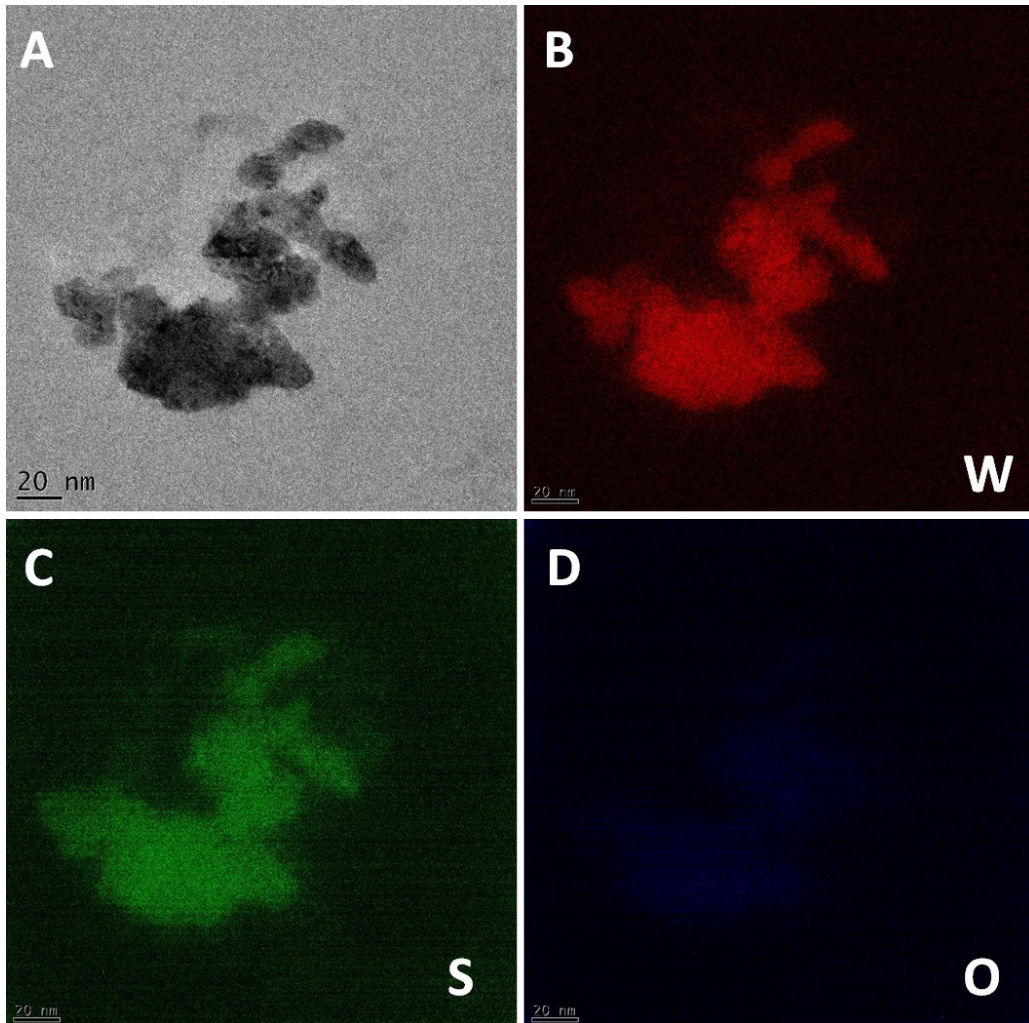


Fig. S3: EELS mapping images of O-WS₂-1T Nano nanoclusters showing different elements (A) Low-resolution TEM image of a nanocluster (B) elemental Tungsten mapping image (C) Sulfur mapping image (D) Oxygen mapping image.

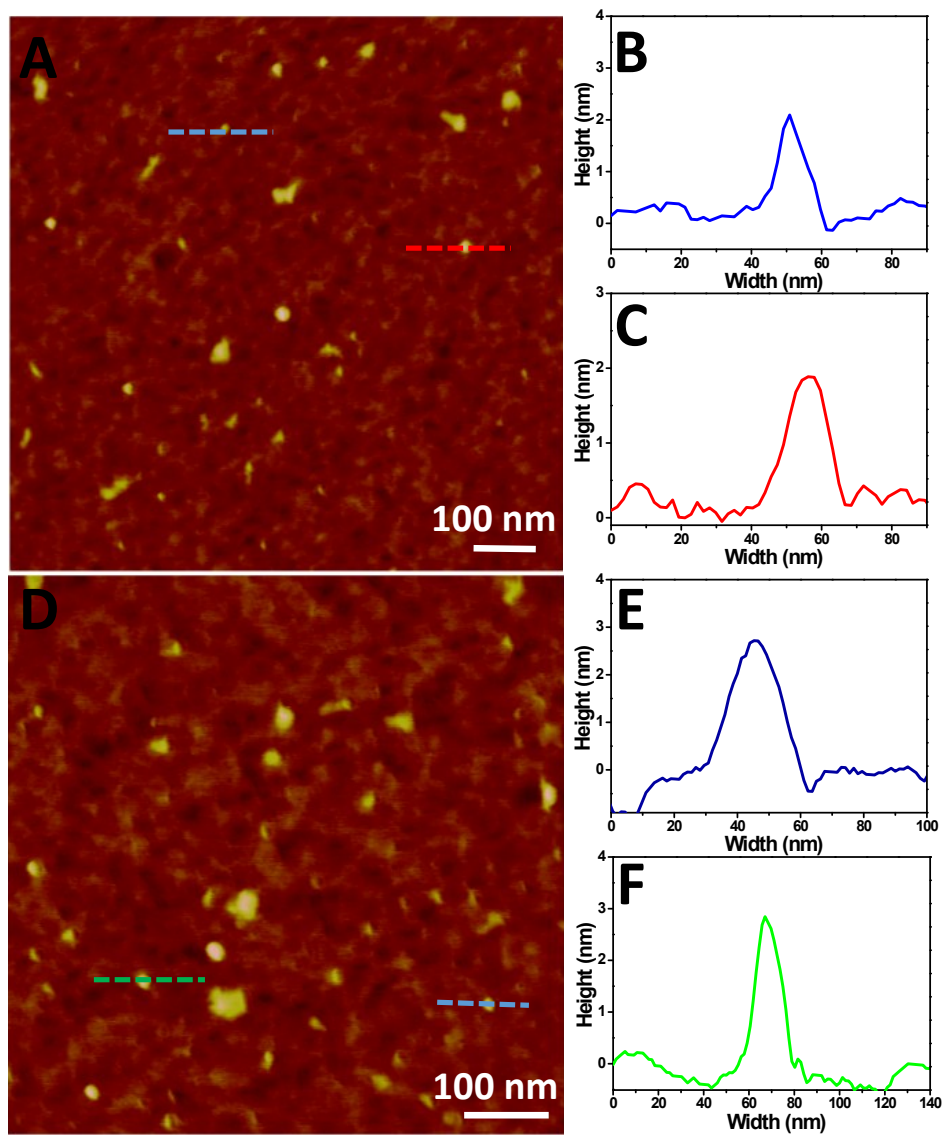


Fig. S4: (A) AFM image O-WS₂-1T nanoclusters. (B) & (C) height profile of the nanoclusters, through the lines drawn on the figure A. In similar fashion, AFM image and the height profile of O-WS₂-2H nanoclusters are shown as figure (D), (E) and (F) respectively. Height profile indicates that the thickness of synthesized nanoclusters is of 2-3 layers only.

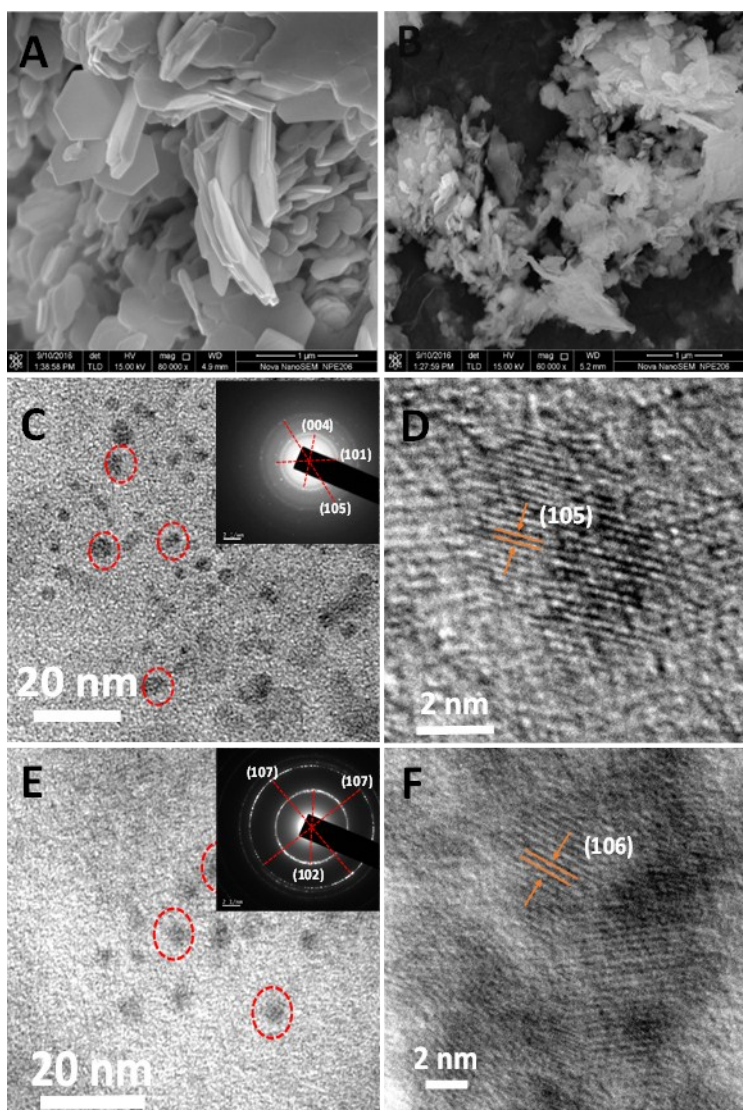


Fig. S5: (A) SEM images of WS₂-Bulk (WS₂-P) powder (B) SEM images of WS₂-P after ball milling (C) TEM (D) HR TEM image of WS₂-BM-1T nanoclusters. (E) TEM (F) HR TEM images of WS₂ -BM-2H nanoclusters. Inset of both (C) and (E) shows SAED pattern from nanoclusters

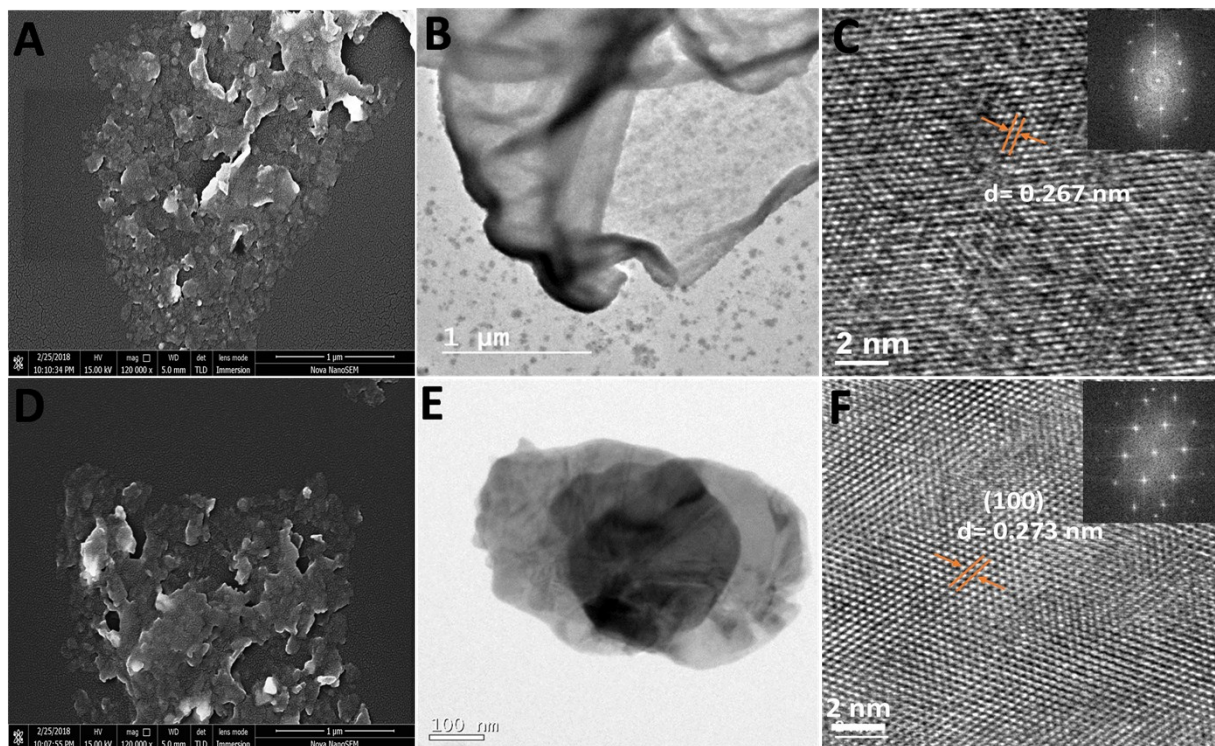


Fig. S6: (A) SEM and (B) TEM images (C) HR TEM images of WS₂-P-1T sheets prepared by Chemical exfoliation (D) SEM and (E) TEM (F) HR TEM images of WS₂-P-2H sheets synthesized by sonication followed by refluxing in DMF

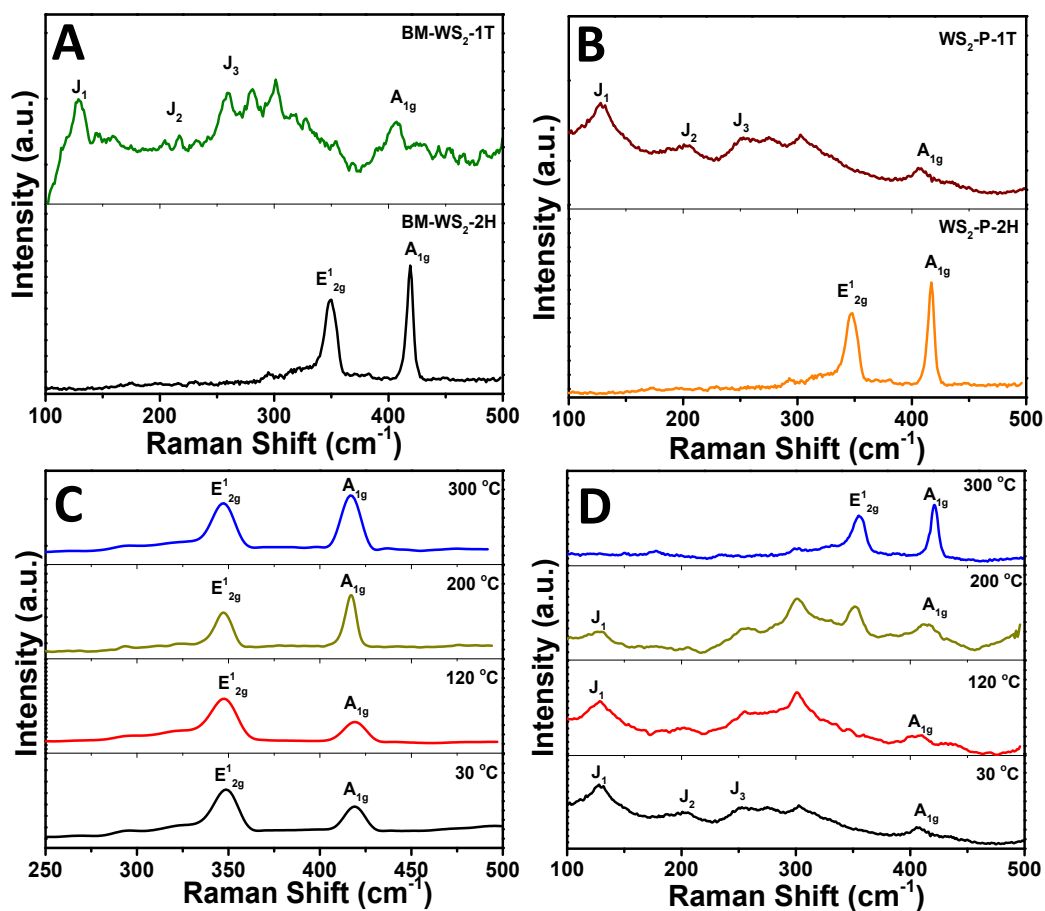


Fig. S7: (A) Raman spectra collected from BM-WS₂-1T and BM-WS₂-2H nanoclusters (B) Raman spectra of 1T and 2H WS₂ sheets (C) & (D) Raman spectra collected from controllably annealed O-WS₂-2H nanoclusters and 1T WS₂ sheets respectively.

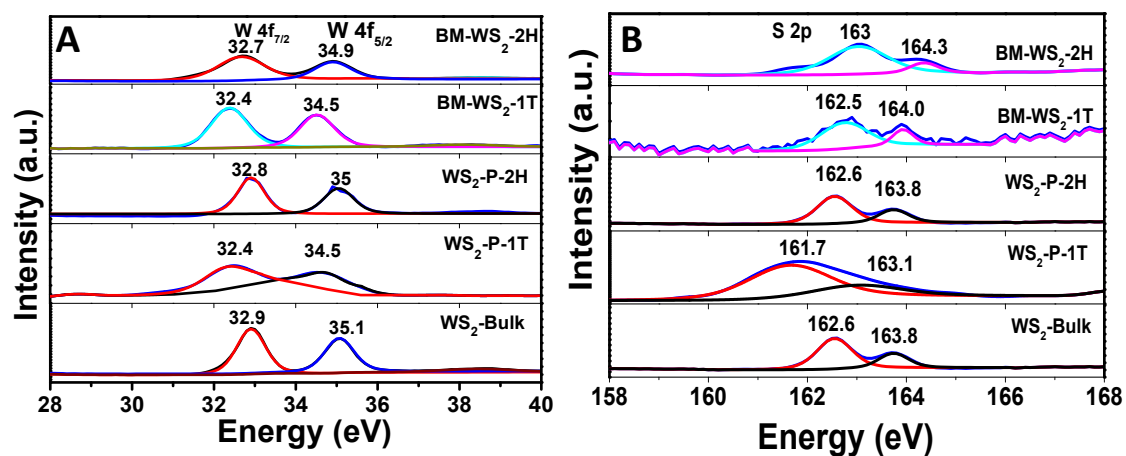


Fig. S8: XPS (A) W 4f spectra (B) S 2p spectra collected from BM-WS₂-1T, BM-WS₂-2H, WS₂-P-2H, WS₂-P-1T and WS₂-Bulk catalysts. All 1T systems showing a considerable shift in W 4f spectra towards lower binding energy compared to their 2H counterpart.

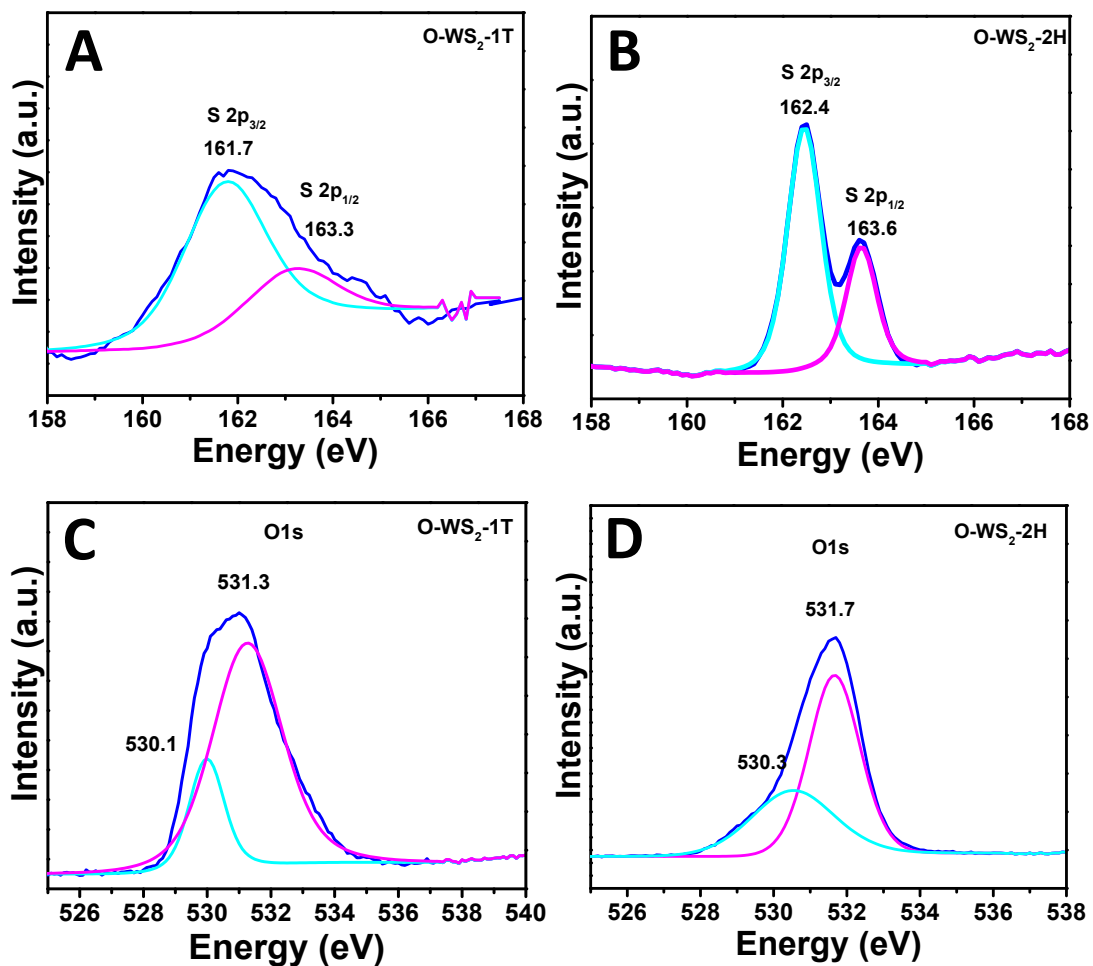


Fig. S9: S 2p XPS spectra collected from (A) O-WS₂-1T nanoclusters (B) O-WS₂-2H nanoclusters. O 1s XPS spectra obtained from (C) O-WS₂-1T nanoclusters (D) O-WS₂-2H nanoclusters.

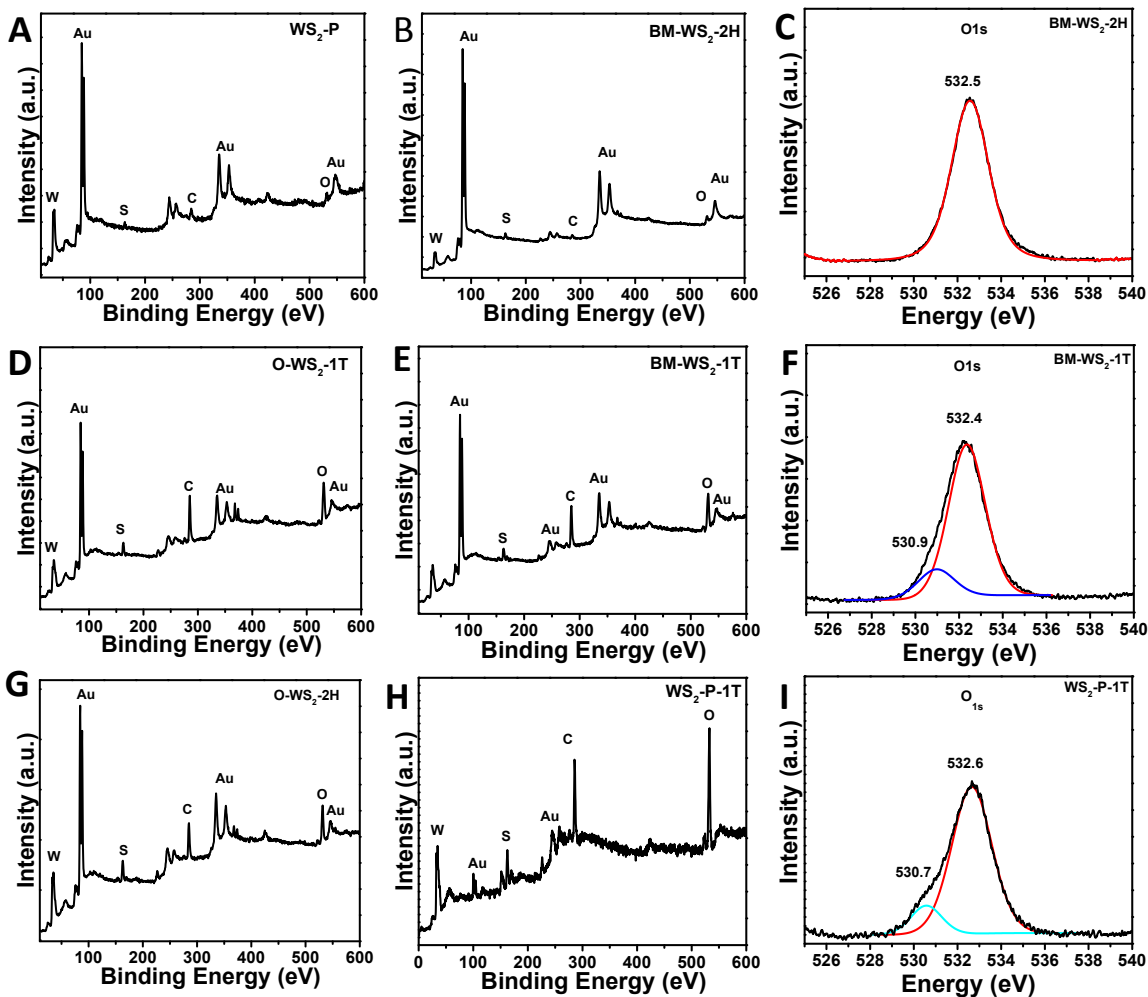


Fig. S10: XPS spectra from (A) WS₂-P (B) BM-WS₂-2H (C) O1s high resolution spectra from BM-WS₂-2H (D) O-WS₂-1T (E) BM-WS₂-2H (F) O1s high resolution spectra from BM-WS₂-1T (G) O-WS₂-2H (H) WS₂-P-1T and (I) O1s high resolution spectra from WS₂-P-1T catalysts. The samples are drop casted on Au substrate for XPS.

Table S1: Detailed information of various catalysts

No.	Catalyst	Size/Area (nm ²)	Edge to basal ratio (%)	R _{CT} at -200 mV (Ω)	Oxygen content (%)
1	WS ₂ -P-1T	4,04,005.0	0.838	41	4.98
2	WS ₂ -P-2H	17,750.0	1.30	98	0
3	BM- WS ₂ -1T	33.20	61.47	11	2.56
4	BM- WS ₂ -2H	29.12	66.58	167	0
5	O-WS ₂ -1T	47.58	50.61	6	8.5
6	O- WS ₂ -2H	34.66	57.14	24	9.9

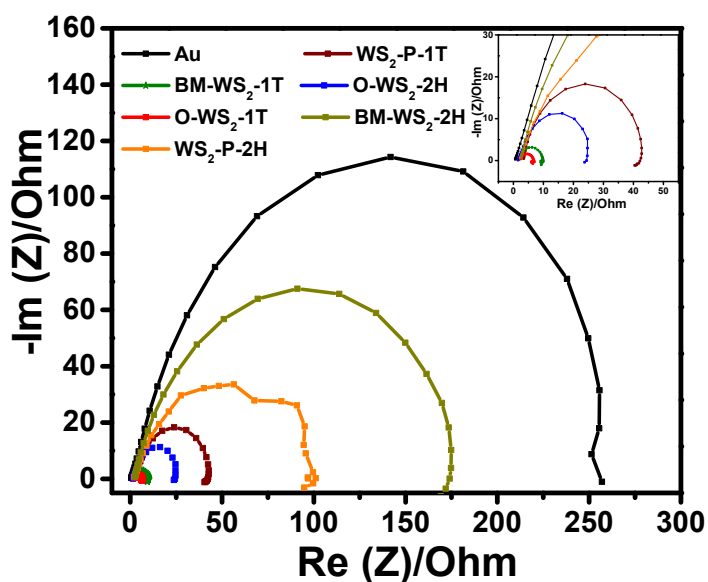


Fig. S11: Potentiostatic EIS spectra from various catalyst under study. Spectra was collected at an over potential of -200 mV vs SHE in 0.5M H₂SO₄ in 3 electrode configuration. Inset shows zoomed portion of EIS spectra.

4. Electrochemical active surface area calculation using cyclic voltammetry

4.a ECSA calculation using 5 mM $K_3[Fe(CN)_6]$ in 0.1 M KCl

We carried out cyclic voltammetry studies to calculate the electro catalytic active surface area of the catalyst and normalize the catalytic activity with respect to active surface area. The cyclic voltammetry is conducted on self assembled monolayers supported on Au substrate in 5mM $[Fe(CN)_6]^{3-/4-}$ redox probe (5 mM $K_3[Fe(CN)_6]$ in 0.1 M KCl). The plot we obtained during CV scan is shown as Supporting Fig. S12. Interestingly, we could not find any oxidation or reduction peaks of Ferricyanide ion in any of the chemically exfoliated 1T catalyst except on bare Au and WS_2 -2H species. This behavior might be due to the negative charge on the adsorbed species (chemically exfoliated catalysts), and because of this negative charge, redox probes are not able to reach the surface of the electrode. Hence, Ferricyanide redox probe is not a suitable species for ECSA calculation in this case. These negatively charges of adsorbed catalyst species may help surface adsorption of H^+ ions during catalysis.

4.b ECSA calculation using Ruthenium hexamine chloride $[Ru(NH_3)_6]^{3+}Cl_3$ in 0.1 M KCl

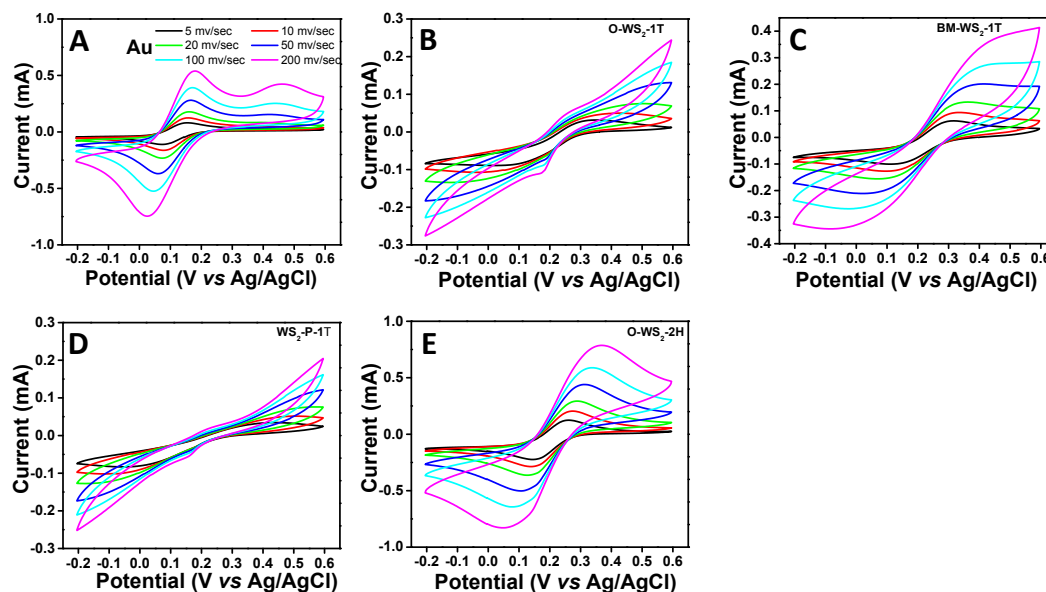


Fig. S12: Cyclic voltammogram recorded for (A) bare Au (B) O- WS_2 -1T (C) BM- WS_2 -1T (D) WS_2 -P-1T (E) O- WS_2 -2H catalyst in 5 mM $K_3[Fe(CN)_6]$ in 0.1 M KCl.

We conducted ECSA calculation using Ruthenium hexamine chloride $[\text{Ru}(\text{NH}_3)_6]^{3+}\text{Cl}_3$ which is positively charged species with a clear redox-oxidation window. The CV curves and calculations were shown in supporting Fig. S13. The electrochemical active surface area was calculated using Randles-Sevcik equation and calculated area was shown in **Table S2**.^[5]

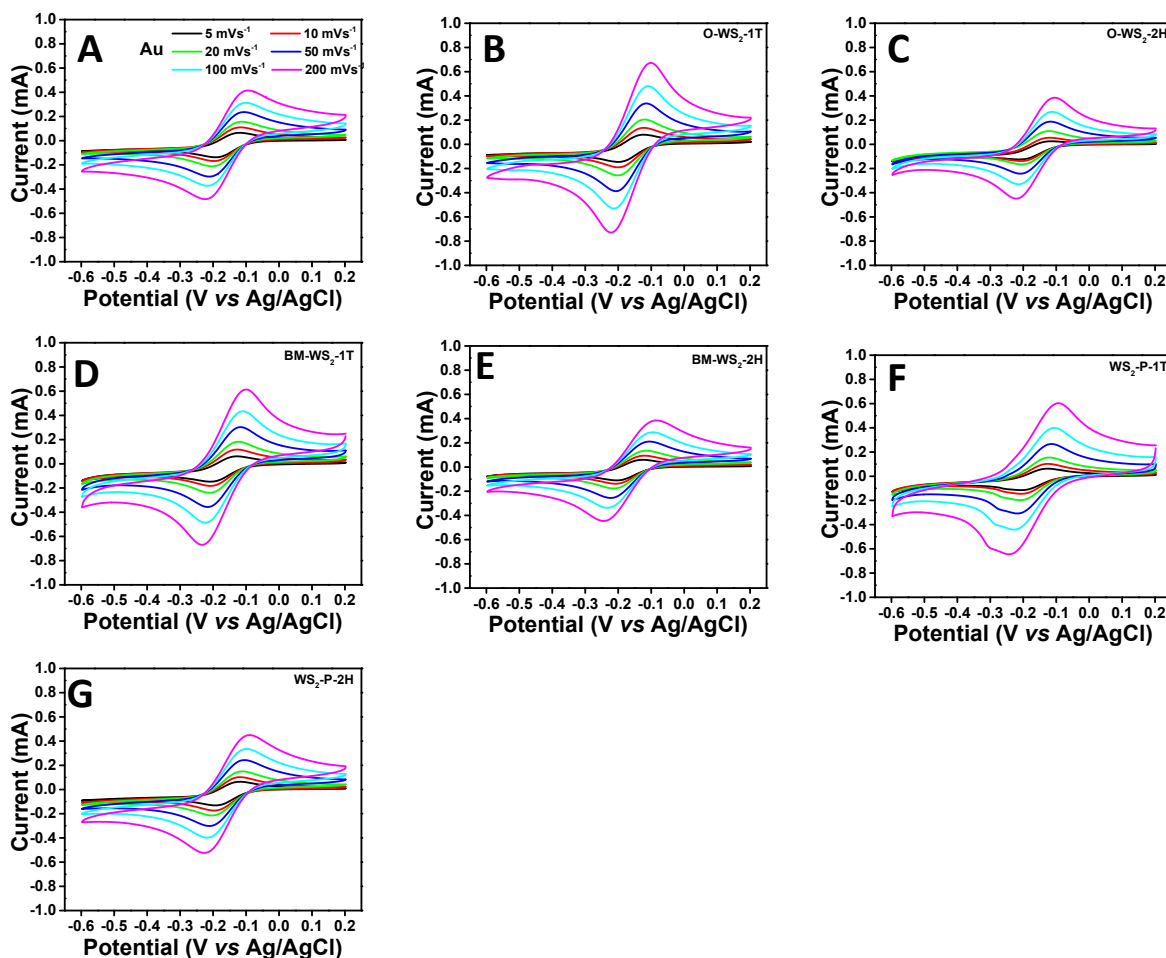


Fig. S13: Cyclic voltammogram plotted for (A) bare Au (B) O-WS₂-1T (C) O-WS₂-2H (D) BM-WS₂-1T (E) BM-WS₂-2H (F) WS₂-P-1T (G) WS₂-P-2H catalysts in 5 mM $[\text{Ru}(\text{CN})_6]^{3+/2+}$ in 0.1 M KCl.

Electrochemical active surface area was calculated using Randles-Sevcik equation that shown below.

$$I_{pa} = (2.69 \times 10^5) n^2 D^{\frac{3}{2}} A v^{\frac{1}{2}} C_{ox}$$

Where v represents the potential scan rate, and C_{ox} is the bulk concentration of the oxidant, n number of electron transfer. The diffusion coefficient (D) is taken as $8.45 \times 10^{-6} \text{ cm}^2\text{s}^{-1}$.^[6] And electrochemical surface area (A) was estimated from the anodic peak current (I_{pa}), obtained in the linear scan voltammogram of $5.0 \text{ mM } [\text{Ru}(\text{NH}_3)_6]^{3+}$ in 0.1 M KCl as a supporting electrolyte. v , scan rate, for this calculations is 200 mVs^{-1} .

Table S2: ECSA values for various catalysts calculated from Randles-Sevcik equation

No.	Catalyst	ECS Area (cm^2)
1	WS ₂ -P-1T	3.737×10^{-4}
2	WS ₂ -P-2H	2.78×10^{-4}
3	BM-WS ₂ -1T	3.803×10^{-4}
4	BM-WS ₂ -2H	2.384×10^{-4}
5	O-WS ₂ -1T	4.167×10^{-4}
6	O-WS ₂ -2H	2.38×10^{-4}

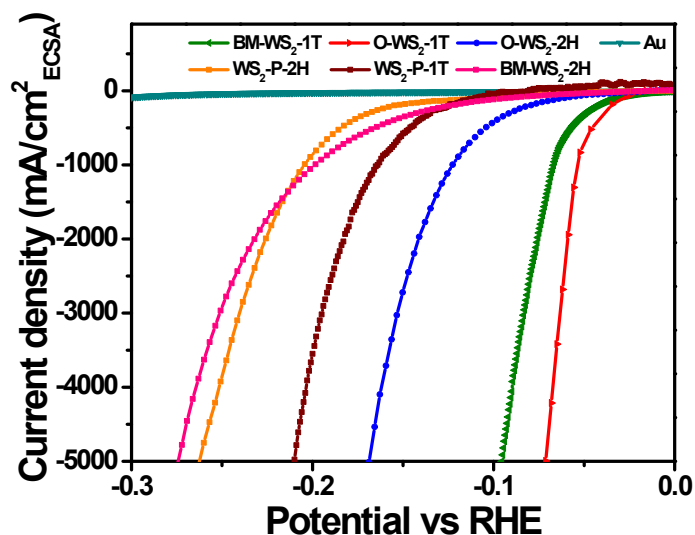


Fig. S14: Polarization curve obtained from various catalyst under this study where current value is normalized using measured electrochemical active surface area calculated using Randles-Sevcik equation.

4.c ECSA calculation through double layer capacitance method

We calculated Electrochemical active surface area using double layer capacitance method. The CV plots with different scan rates were shown as Supporting Fig. S15. We plotted ΔJ (Ja-Jc) current at a potential (0.2V vs SHE) against scan rate and electric double layer capacitance (EDLC) is counted as half of the slope of this line. Since self-assembly happens on a plane

surface, active surface area was calculated as $A_{ECSA} = \frac{C_{DL-Catalyst}}{C_{DL-Substrate}}$ where $C_{DL-Catalyst}$ and $C_{DL-Substrate}$ are EDLC values of Catalyst and substrate respectively.^[7-8]

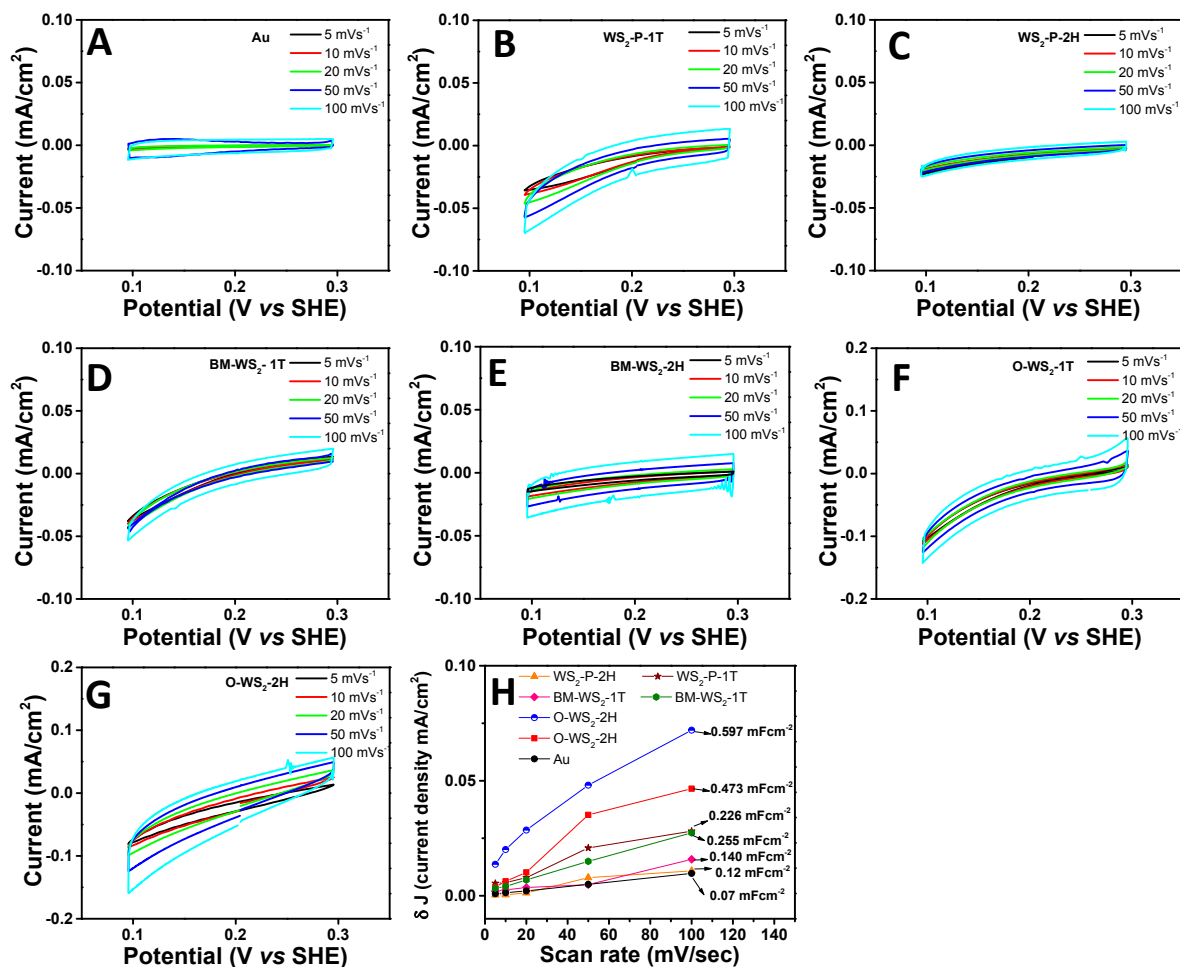


Fig. S15: (A)-(G) Double layer capacitance value obtained for various catalyst under this study (Self assembled monolayers of catalyst on Au substrate) in 0.5M H₂SO₄ electrolyte in 3 electrode configuration, (H) ΔJ (Ja-Jc) current at a potential (0.2V vs SHE) against scan rate.

The calculated values of C_{DL} where shown as Table S4.

Table S3: Double layer capacitance and electrochemical surface area calculated from double layer capacitance method for various catalysts under study

No.	Catalyst	C_{DL} (mF/cm ²)	A_{ECSA}
1	Au	0.035	1
2	WS ₂ -P-1T	0.113	3.22
3	WS ₂ -P-2H	0.060	1.714
4	BM-WS ₂ -1T	0.127	3.64
5	BM-WS ₂ -2H	0.070	2
6	O-WS ₂ -1T	0.236	6.75
7	O-WS ₂ -2H	0.289	8.271

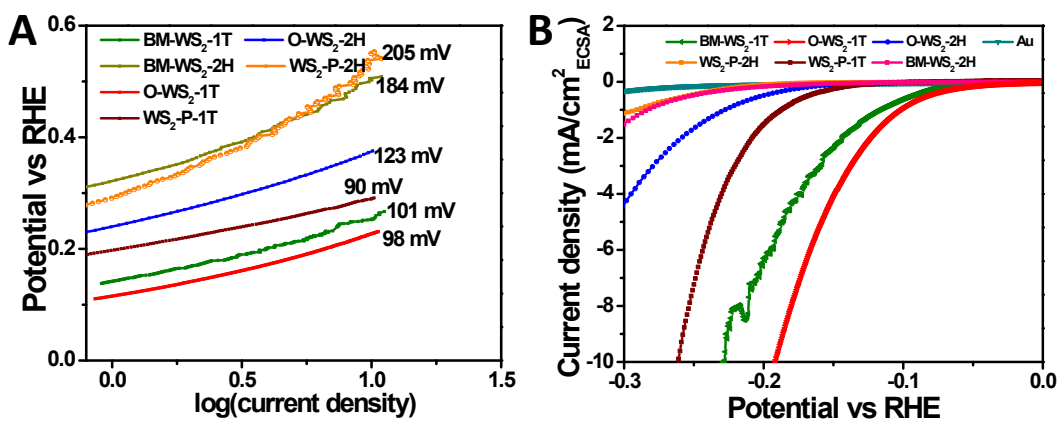


Fig. S16: (A) Tafel plots and (B) polarization curves obtained for various catalyst where current was normalized by electrochemical surface area calculated through double layer capacitance method.

Table S4: Tafel slope and exchange current density calculated from ECSA normalized polarization curve.

No.	Catalyst	Tafel slope (mV dec ⁻¹)	Exchange current density (mA cm ⁻²)
1	WS ₂ -P-1T	90	0.125 x 10 ⁻²
2	WS ₂ -P-2H	205	0.105 x 10 ⁻²
3	BM-WS ₂ -1T	101	1.40 x 10 ⁻²
4	BM-WS ₂ -2H	184	0.31 x 10 ⁻²
5	O-WS ₂ -1T	98	2.5 x 10 ⁻²
6	O-WS ₂ -2H	123	0.8 x 10 ⁻²

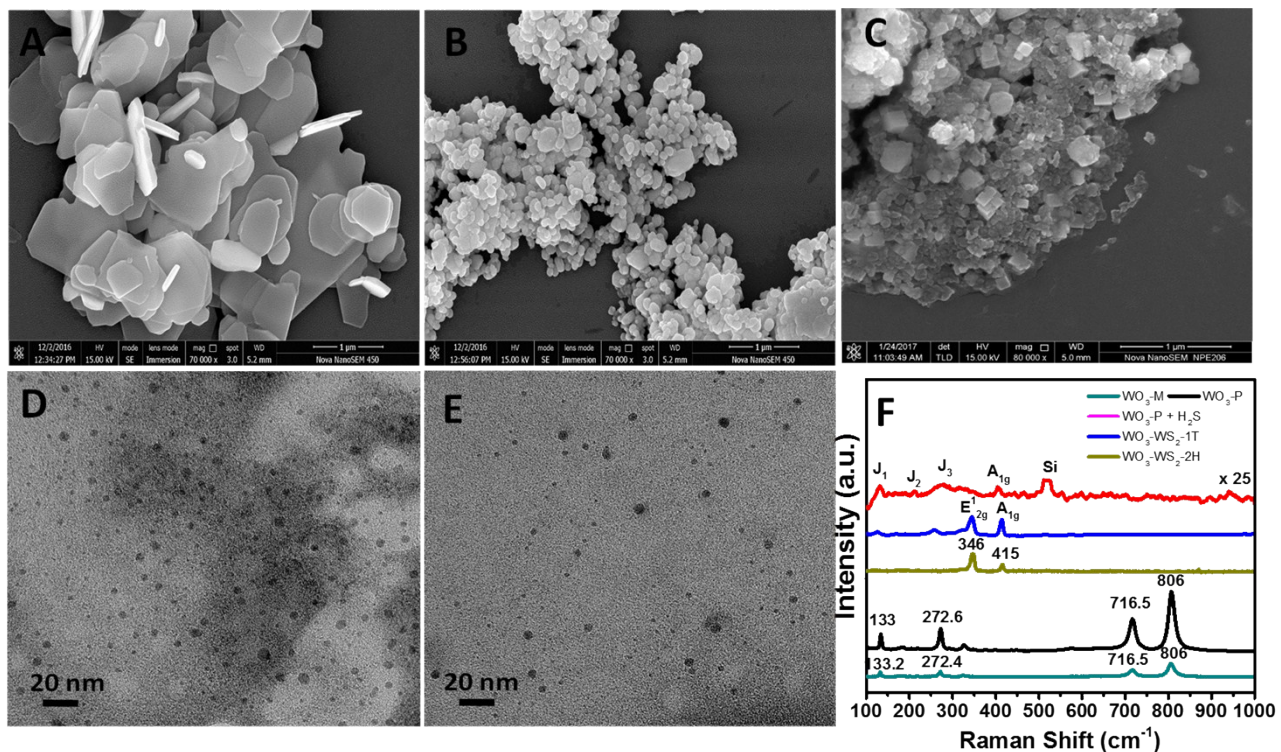


Fig. S17: (A) & (B) SEM image of WO₃ Pristine powder before and after ball milling. (C) SEM image of H₂S treatment of ball milled WO₃-P Powder. (D) Low-resolution TEM images of WO₃-WS₂-1T. (E) WO₃-WS₂-2H nanoclusters. (F) Raman spectra collected from WO₃-P, milled and H₂S treated sample (WO₃-WS₂), WO₃-WS₂-1T and 2H nanoclusters.

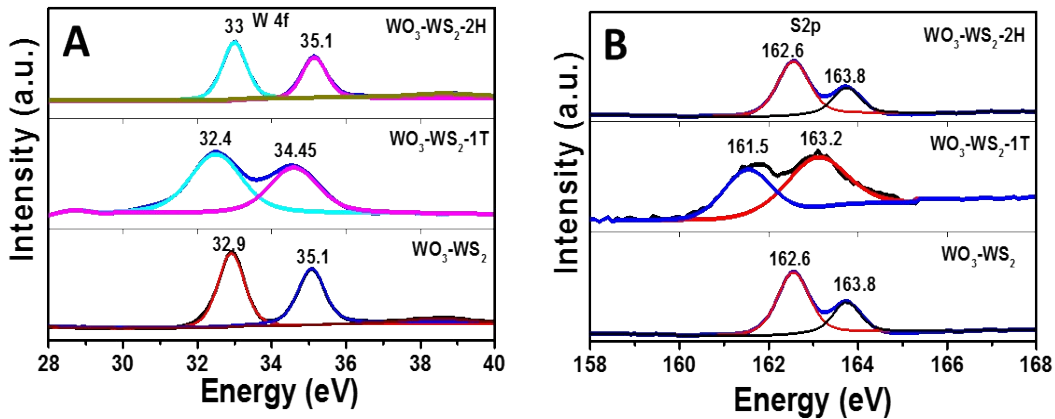


Fig. S18: (A) W 4f (B) S 2p XPS spectra collected from $\text{WO}_3\text{-WS}_2\text{-2H}$, $\text{WO}_3\text{-WS}_2\text{-1T}$ and $\text{WO}_3\text{-WS}_2$ samples respectively.

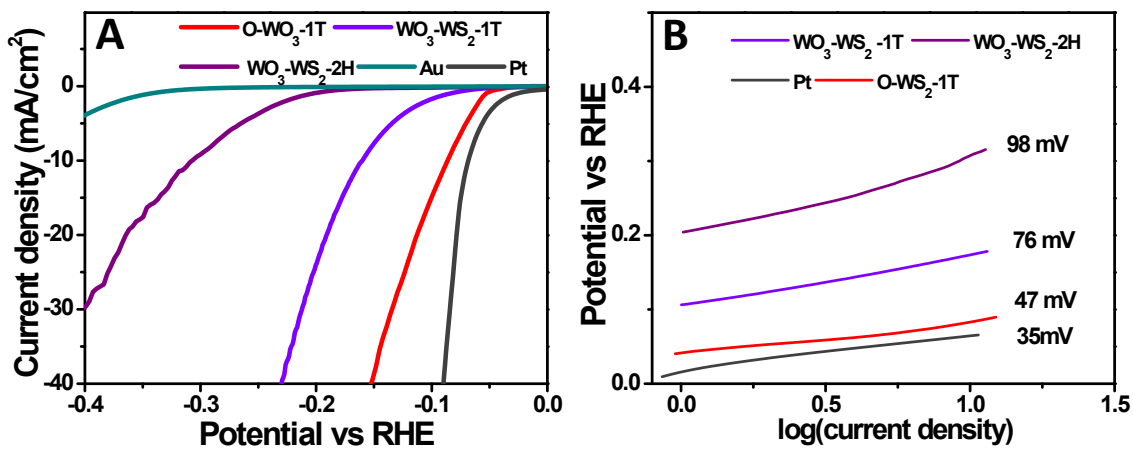


Fig. S19: (A) Polarization and (B) Tafel plot obtained from $\text{WO}_3\text{-WS}_2\text{-1T}$, $\text{WO}_3\text{-WS}_2\text{-2H}$, Platinum and $\text{O-WO}_3\text{-1T}$ catalysts.

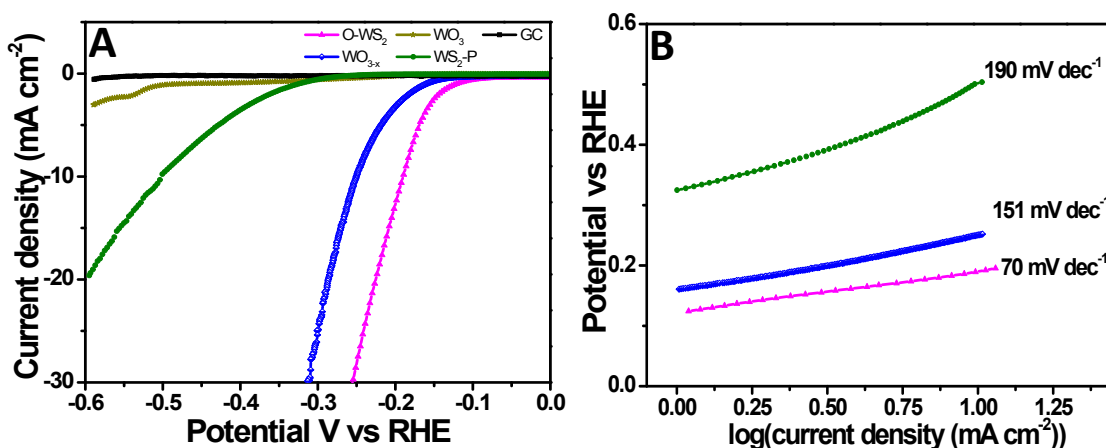


Fig. S20: (A) Polarization (B) Tafel plot obtained from WO₃ pristine, WS₂ pristine, WO_{3-x} and O-WS₂ samples.

References

1. H. A. Therese, J. Li, U. Kolb and W. Tremel, *Solid State Sci.*, 2005, **7**, 67-72.
2. M. Dieterle, G. Weinberg and G. Mestl, *Phys. Chem. Chem. Phys.*, 2002, **4**, 812-821.
3. S.-H. Lee, M. J. Seong, H. M. Cheong, E. Ozkan, E. C. Tracy and S. K. Deb, *Solid State Ionics*, 2003, **156**, 447-452.
4. F. Y. Xie, L. Gong, X. Liu, Y. T. Tao, W. H. Zhang, S. H. Chen, H. Meng and J. Chen, *Journal of Electron Spectroscopy and Related Phenomena*, 2012, **185**, 112-118.
5. M. Remškar, J. Kovac, M. Viršek, M. Mrak, A. Jesih and A. Seabaugh, *Adv. Funct. Mater.*, 2007, **17**, 1974-1978.
6. M. Seifollahi Bazarjani, M. Hojamberdiev, K. Morita, G. Zhu, G. Cherkashinin, C. Fasel, T. Herrmann, H. Breitzke, A. Gurlo and R. Riedel, *J. Am. Chem. Soc.*, 2013, **135**, 4467-4475.
7. R. F. Garcia-Sanchez, T. Ahmido, D. Casimir, S. Baliga and P. Misra, *J. Phys. Chem. A*, 2013, **117**, 13825-13831.
8. Z. Luo, R. Miao, T. D. Huan, I. M. Mosa, A. S. Poyraz, W. Zhong, J. E. Cloud, D. A. Kriz, S. Thanneeru, J. He, Y. Zhang, R. Ramprasad and S. L. Suib, *Adv. Energy Mater.*, 2016, **6**, 1600528-n/a.
9. Y. Baek and K. Yong, *J. Phys. Chem. C*, 2007, **111**, 1213-1218.
10. N. Minh Vuong, D. Kim and H. Kim, *Scientific Reports*, 2015, **5**, 11040.
11. A. Berkdemir, H. R. Gutiérrez, A. R. Botello-Méndez, N. Perea-López, A. L. Elías, C.-I. Chia, B. Wang, V. H. Crespi, F. López-Urías, J.-C. Charlier, H. Terrones and M. Terrones, *Sci. Rep.*, 2013, **3**, 1755.
12. Q. Liu, X. Li, Z. Xiao, Y. Zhou, H. Chen, A. Khalil, T. Xiang, J. Xu, W. Chu, X. Wu, J. Yang, C. Wang, Y. Xiong, C. Jin, P. M. Ajayan and L. Song, *Adv. Mater.*, 2015, **27**, 4837-4844.

13. U. Gupta, B. S. Naidu, U. Maitra, A. Singh, S. N. Shirodkar, U. V. Waghmare and C. N. R. Rao, *APL Materials*, 2014, **2**, 092802.